Draft version August 28, 2023
Typeset using LaTeX **manuscript** style in AASTeX631

Analyses of ∼ 0.05-2 MeV ions associated with the 2022 February 16 ESP Event Observed by Parker Solar Probe*

Joe Giacalone,[1] C. M. S. Cohen,[2] D. J. McComas,[3] X. Chen,[1] M. A. Dayeh,[4,5] W. H. Matthaeus,[6] K. G. Klein,[1] S. D. Bale,[7] E. R. Christian,[8] M. I. Desai,[4,5] M. E. Hill,[9] L. Y. Khoo,[3] D. Lario,[8] R. A. Leske,[2] R. L. McNutt Jr.,[9] D. G. Mitchell,[9] J. G. Mitchell.,[8] O. Malandraki,[10] and N. A. Schwadron[11,3]

[1] *Lunar & Planetary Laboratory, University of Arizona, Tucson, AZ 85721, USA*

[2] *California Institute of Technology, Pasadena, CA 91125, USA*

[3] *Department of Astrophysical Sciences, Princeton University, Princeton, NJ, 08544, USA*

[4] *Southwest Research Institute, San Antonio, TX 78238, USA*

[5] *University of Texas at San Antonio, San Antonio, TX 78249, USA*

[6] *University of Delaware, Newark, DE 19716, USA*

[7] *Physics Department, University of California at Berkeley, Berkeley, CA 94720-7300, USA*

[8] *Heliophysics Science Division, NASA/Goddard Space Flight Center, Greenbelt, MD 20771, USA*

[9] *Applied Physics Laboratory, Laurel, MD 20723, USA*

[10] *Institute for Astronomy, Astrophysics, Space Applications Remote Sensing, National Observatory of Athens, Greece*

[11] *University of New Hampshire, Durham, NH, 03824, USA*

ABSTRACT

We present analyses of 0.05 - 2 MeV ions from the 16 Feb 2022 energetic storm particle (ESP) event observed by Parker Solar Probe's (PSP) IS⊙IS/EPI-Lo instrument at 0.35 au from the Sun. This event was characterized by an enhancement in ion fluxes from a quiet background, increasing gradually with time with a nearly flat spectrum, rising sharply near the arrival of the coronal-mass ejection (CME) driven shock, be-

Corresponding author: J. Giacalone
giacalon@lpl.arizona.edu

* Released to co-authors for comments on May, 19th, 2023

coming nearly a power-law spectrum, then decaying exponentially afterwards, with a rate that was independent of energy. From the observed fluxes, we determine diffusion coefficients, finding that far upstream of the shock the diffusion coefficients are nearly independent of energy with a value of 10^{20} cm^2/s. Near the shock, the diffusion coefficients are more than one order of magnitude smaller and increase nearly linearly with energy. We also determine the source of energetic particles, by comparing ratios of the intensities at the shock to estimates of the quiet time intensity to predictions from diffusive shock acceleration theory. We conclude that the source of energetic ions is mostly the solar wind for this event. We also present possible interpretations of the near-exponential decay of the intensity behind the shock. One is that we suggest the shock was over-expanding when it crossed PSP and the energetic particle intensity decreased behind the shock to fill the expanding volume. Over-expanding CMEs could well be more common closer to the Sun, and this is an example of such a case.

1. INTRODUCTION

Solar energetic particles (SEPs) are high-energy charged nuclei associated with processes occurring at the Sun. The term SEP is a broad categorization. They can be related to solar flares, even small ones, transient disturbances in the solar wind plasma, and interactions between high-speed and low-speed solar wind flows leading to corotating interaction regions. The SEP events of the highest intensity are well correlated with the occurrence of coronal mass ejections (CME) (Gosling 1993). At energies below a few MeV/nuc., the arrival of a CME-driven shock at the spacecraft can be accompanied by ion intensity increases (c.f. Giacalone 2012), and these are given the term "energetic storm particle" (ESP) events (Bryant et al. 1962). A common characteristic of ESP events is that the particle intensity increases abruptly from the background several hours, even up to a day or so before the arrival of the shock, and then increase gradually until 15-30-minutes prior to the arrival of the shock itself where the intensities rise again very abruptly (c.f. Reames 1999; Giacalone 2012, and references therein). Sometimes, during the gradual-rise phase of ESP events, the fluxes of energetic ions are very nearly the same, and rise at the same rate (Lario et al. 2018). These produce very nearly flat energy spectra. This phenomenon is not presently well understood, but may be related to the way in which particles escape from near the shock where they are confined by turbulent magnetic fields (Perri et al. 2023), adiabatic cooling (Prinsloo et al. 2019), or perhaps a balance between the injection rate (at very low energies) at the shock, and their escape upstream (Lario et al. 2018).

ESP events are excellent targets for studying the physics of particle acceleration and transport. For instance, the occurrence of these events provides a unique opportunity to directly determine transport coefficients (e.g. Beeck & Sanderson 1989; Tan et al. 1989; Gloeckler et al. 1985; Giacalone 2012). In addition, these events are generally associated with very high particle intensities providing excellent counting statistics. This permits an event-based analysis on determining the source of the material being accelerated by the shock by comparing the distribution function at very low energies, including the thermal particles, just prior to and after the crossing of the shock. This was discussed by Guo et al. (2021) who analysed the DOY 118, 2001 ESP event (c.f. Lario et al. 2019) seen by the *Advanced Composition Explorer*, and concluded the high-energy protons must have originated as solar wind protons that were accelerated directly at the shock.

Parker Solar Probe (PSP), launched in 2018 (Fox et al. 2016), has a highly elliptical in-the-ecliptic orbit allowing for a sampling of the solar wind, magnetic field, and energetic particles over a range of heliocentric distances from ~ 0.02AU to ~ 0.7AU. It has observed a number of CME-related SEP events (e.g., McComas et al. 2019; Raouafi et al. 2023; Giacalone et al. 2020, 2021; Cohen et al. 2021; Lario et al. 2021) at a variety of heliocentric distances. In this paper, we present analyses of another ESP event recently observed by PSP that occurred on 16 Feb, 2022. This event displayed a quasi-flat energy spectrum upstream of the shock. In addition to the evolution of the energy spectrum across the shock, we also use observations from the EPI-Lo instrument (McComas et al. 2016; Hill et al. 2017) which is part of the Integrated Science Investigation of the Sun (IS$\odot$IS) (McComas et al. 2016), to determine transport coefficients of the energetic ions. This event was also characterised by a near-exponential decay in the particle intensities behind the shock with the same rate of decrease over a wide range of energies. We describe a few scenarios that may lead to such behavior. We also discuss the source of the accelerated particles for this event, presenting an analysis based on comparing the ratio of the peak intensity at a given energy at the time of the shock passage to an upper bound on the background intensity at the same energy with the prediction of diffusive shock acceleration theory. This event was associated with a significant increase in the intensity of energetic ions to permit such an analysis.

2. OBSERVATIONS

In this study we analyze 1-minute resolution PSP/IS⊙IS/EPI-Lo ion intensities (c.f. McComas et al. 2016; Hill et al. 2017). We use both the ChanP (protons) and ChanC (He and O ions) data products in this study. We also use 1-second resolution magnetic-field measurements from the FIELDS instrument (Bale et al. 2016) for contextual information, such as the timing of the passage of the shock, the arrival of the interplanetary coronal mass ejection (ICME), and the general nature of the direction of the magnetic field for this event. Additional contextual solar wind velocity vector and ion number density data from the SWEAP instrument (Kasper et al. 2016) are also used.

Figure 1 shows an overview of the ESP event that occurred on 16 Feb, 2022. The top panel shows the magnetic field vector magnitude and RTN coordinates, while the bottom two panels show $\sim 0.05 - 5$ MeV proton intensities. The middle panel shows time-intensity profiles at some selected energies, as indicated at the right, while the bottom panel show all of the energies, with the intensity represented with the color scale. At this time, PSP was located about 0.35au from the Sun. The solar eruption associated with the origin of this event has been analyzed by Mierla et al. (2022). Although it is not shown in this paper, analysis of STEREO-A (STA) Cor 2 images reveal that a CME appeared in the instrument's field of view at 22:23:30UT on 2022 Feb 15. The central bright part of the CME was seen to be moving northward relative to the ecliptic plane, at a latitude of some $\sim$45 degrees. The CME had a relatively large latitudinal extent. Based on the relative locations of PSP and STEREO-A during this time, it is clear the CME was moving towards PSP. The magnetic field shown in the top panel of Figure 1 reveals that PSP observed a large-scale magnetic flux rope, suggesting that PSP was indeed crossed by the CME. **In Section 4, we discuss the results from a ENLIL numerical simulation of this event, including a CME from the so-called "cone**

model", which required an initial speed of about 2500 km/s in order for the model to give a time of arrival consistent with that observed. As we discuss in the next section, we find than the shock assocaited with this CME was moving considerably slower than this, suggesting the shock had slowed considerably between the Sun and PSP. The SEP event itself is qualitatively similar to ESP events seen previously in that there is a gradual increase in the particle flux prior to the arrival of the CME, which rises rapidly and peaks at the passage of the CME-driven shock, followed by a quasi-constant, or gradual decay in flux in the CME-sheath region, then followed by a significant depletion within the flux rope itself (indicated by the dashed line labeled ICME in Figure 1). The timing of the CME appearance in the STA-Cor2 image, the shock arrival, and the ICME flux-rope arrival are indicated with vertical dashed lines in the figure.

Figure 1 also indicates two noteworthy periods. One is the gradual increase in particle intensity prior to the shock arrival for which the intensity is nearly the same at all energies shown. This corresponds to a "flat spectra" period. This phenomenon has been seen in some SEP events observed by near-Earth spacecraft (Lario et al. 2018). To our knowledge, this is the first such observation by PSP reported to date, and, may represent the closest such observation to the Sun to date. We also identify a period of time after the shock arrival in which the intensity of energetic protons decreases with essentially the same rate at all energies. This represents a dispersionless decay in particle intensity. We discuss this further in Section 3.3.

2.1. *Energy Spectra*

Figure 2 shows the energy spectrum for this event for three different time periods as indicated in the legend at the lower left of the image (in units of decimal day of year 2002), using the ChanP data product. The highest energy at which the ESP event produced an increase appears to be about 2 MeV, since the three spectra match at energies above this. The dashed lines are representative power laws with two different spectral indices, as indicated. The spectra shown with the blue lines and symbols is that just at the peak of the ESP event, and slightly downstream of the shock. For the energy range $\sim$ 0.2-1MeV, the spectrum is close to a power law with a spectral index of about -1.6. At energies below about 100 keV, the spectra turns upward and is somewhat steeper. The

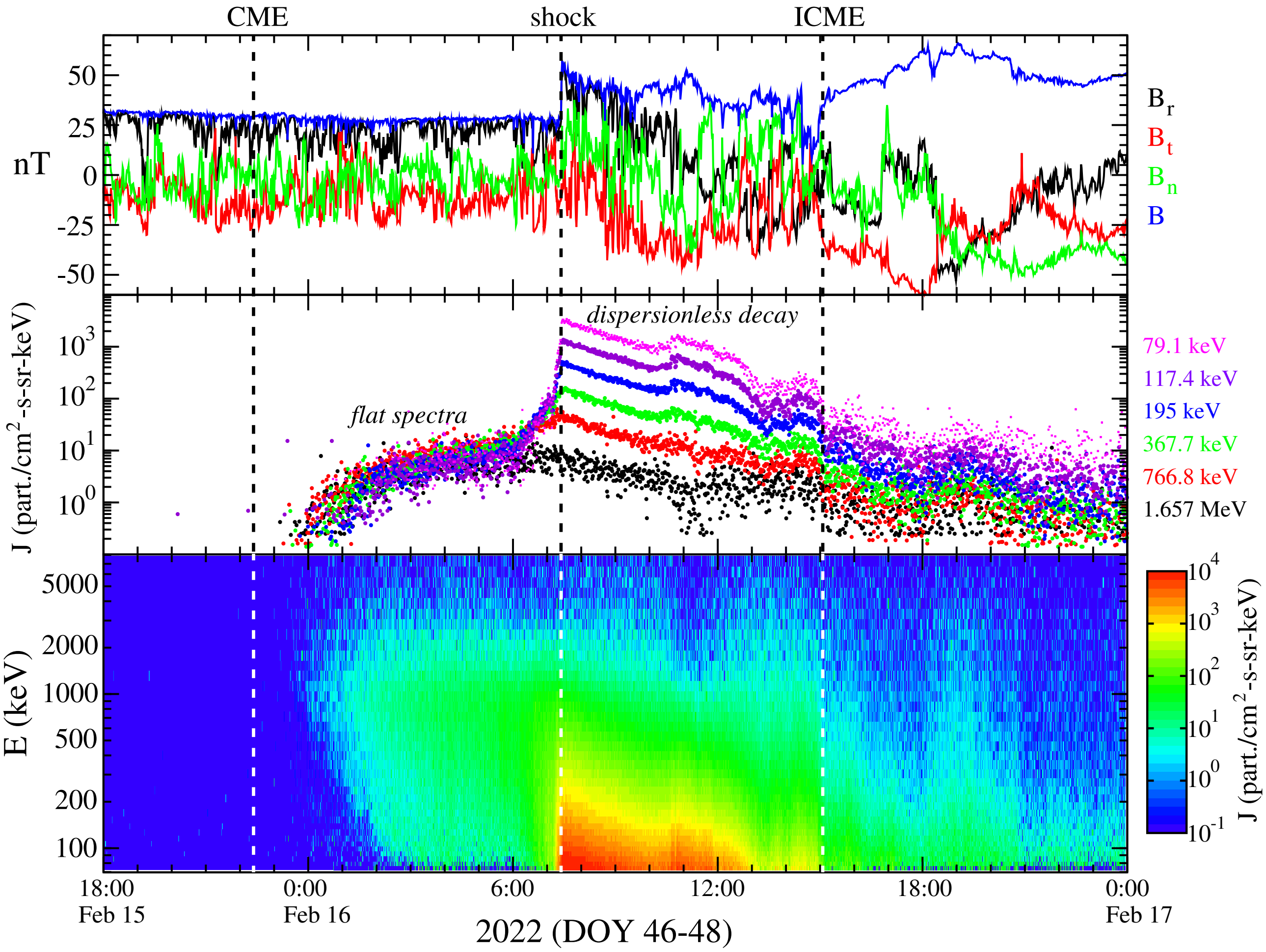

Figure 1. Overview of observations of the SEP event observed by PSP on Feb 16, 2022. The top panel shows the magnetic field vector, with components represented by colors as indicated at the right of the panel, the middle panel shows differential intensity of energetic protons, with energies indicated at the right of the panel, and the bottom panel shows the differential intensity, represented as a color spectogram, of all protons in our study with energy along the vertical axis. The vertical dashed lines represent the time of significant events. The one on the left is the time in which STEREO-A/Cor2 first observed the CME, and middle one represents the arrival of the shock, and the far right one is the onset of the magnetic flux rope associated with the ICME.

cause of this is not presently understood. At energies above about 1 MeV, the spectrum steepens slightly to another power law with a spectral index closer to -2. The harder power law is likely the result of the acceleration of particles at the shock. In the theory of diffusive shock acceleration, a power-law spectrum is predicted for the shock and downstream region with a spectral index that

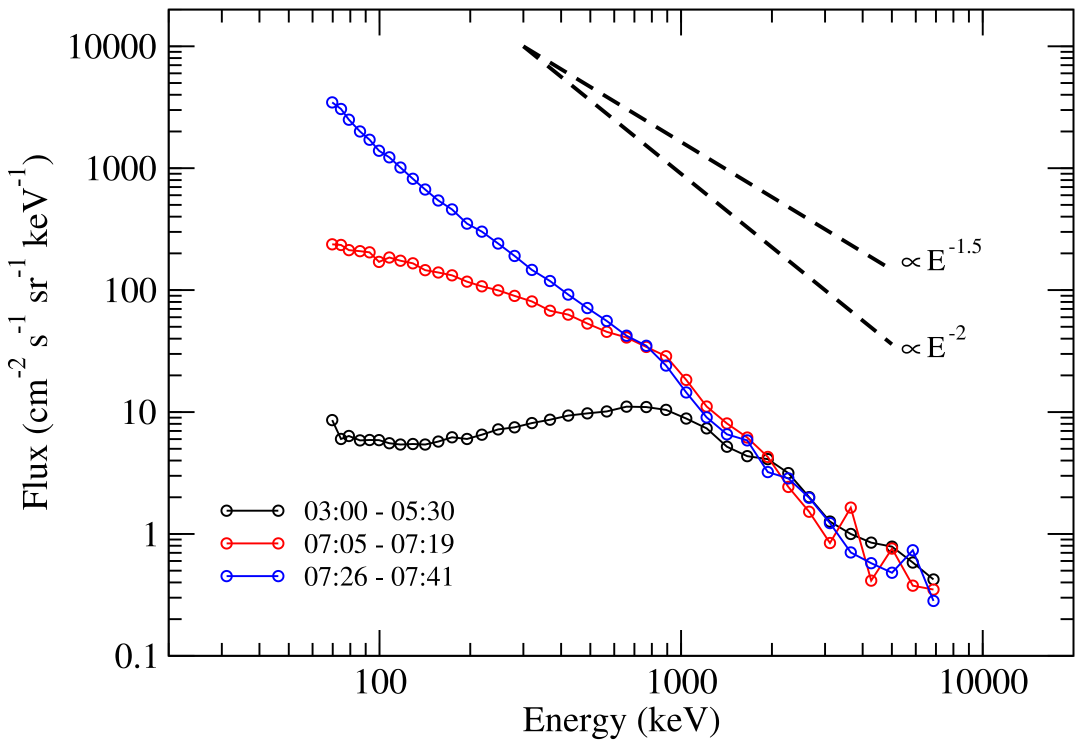

Figure 2. Energy spectra of energetic protons for this SEP event taken over three separate time intervals, as indicated in the legend at the lower left of the figure. The dashed lines are representative power-law distributions as a guide.

depends only on the plasma density jump at the shock. A differential intensity spectrum with a power-law dependence on energy with a -1.6 index corresponds to a density jump of about 2.4. Later we show plasma density for this event, and it is difficult to determine a precise value of the density jump due to significant variations in the density upstream of the shock, but a value of 2.4 is generally consistent with the observations. The plasma density variation across the shock is discussed later in Section 4.

The spectrum shown with the black symbols and solid lines corresponds to the period identified in Figure 1 as the flat spectra period. We see that this spectrum below $\sim$ 1 MeV is not perfectly flat, but is certainly flatter than it is during the rise phase at the shock (red symbols and connecting solid lines), and at the shock and downstream (blue). It is also noteworthy that the spectrum very near, but upstream of the shock (red circles and lines), has two separate power laws: a harder one for energies below ∼1 MeV, and steeper above this energy.

3. ANALYSES

3.1. *Determination of Diffusion Coefficients*

By inspection of Figure 1b, during the period of time associated with the nearly flat energy spectrum, the particle intensities rise very slowly with time. The fluxes are enhanced well above the background by at least an order of magnitude or more, but it is also clear that there are considerable fluctuations about an average value, presumably caused by poor statistics. Closer to the shock, starting just after **6:00 UT on DOY 47**, the fluxes rise quite dramatically. The time scales of the intensity rise during these two time periods can be used to estimate diffusion coefficients, assuming the transport is diffusive, and that their increase in intensity is the result of the approaching the shock, which is where the intensity reaches a maximum. The change from a gradual increase in the particle intensity to a rapid one suggests the diffusion coefficient is a function of distance from the shock, being larger far upstream from the shock, and smaller closer to it. We note that using the intensity increase of energetic ions upstream of shocks has been used in previous studies to estimate the diffusion coefficient, or mean-free path of the particles (e.g. Beeck & Sanderson 1989; Tan et al. 1989; Giacalone 2012; Wijsen et al. 2022).

We select two separate time periods upstream of the shock to perform our analysis of the diffusion coefficient. The first is a ∼3.6-hr period from **2:30UT to 6:00UT on DOY 47**. We refer to this region as "far upstream of the shock". The second region is from **7:11UT to 7:26UT on DOY 47, a period of about** 15 minutes. We average the data over a few energy bins in order to improve statistics. The time-intensity profiles are shown in Figure 3. For the interval far upstream of the shock, we show four energy ranges, as indicated in the figure caption (see also Table 1), in four separate panels. For the interval closer to the shock, we show all four energies on the same right-panel plot. The black lines in each of these figures are the least-squares fit to the data. Table 1 gives the exponential rise time, Δt, associated with each of these fits, as well as each correlation

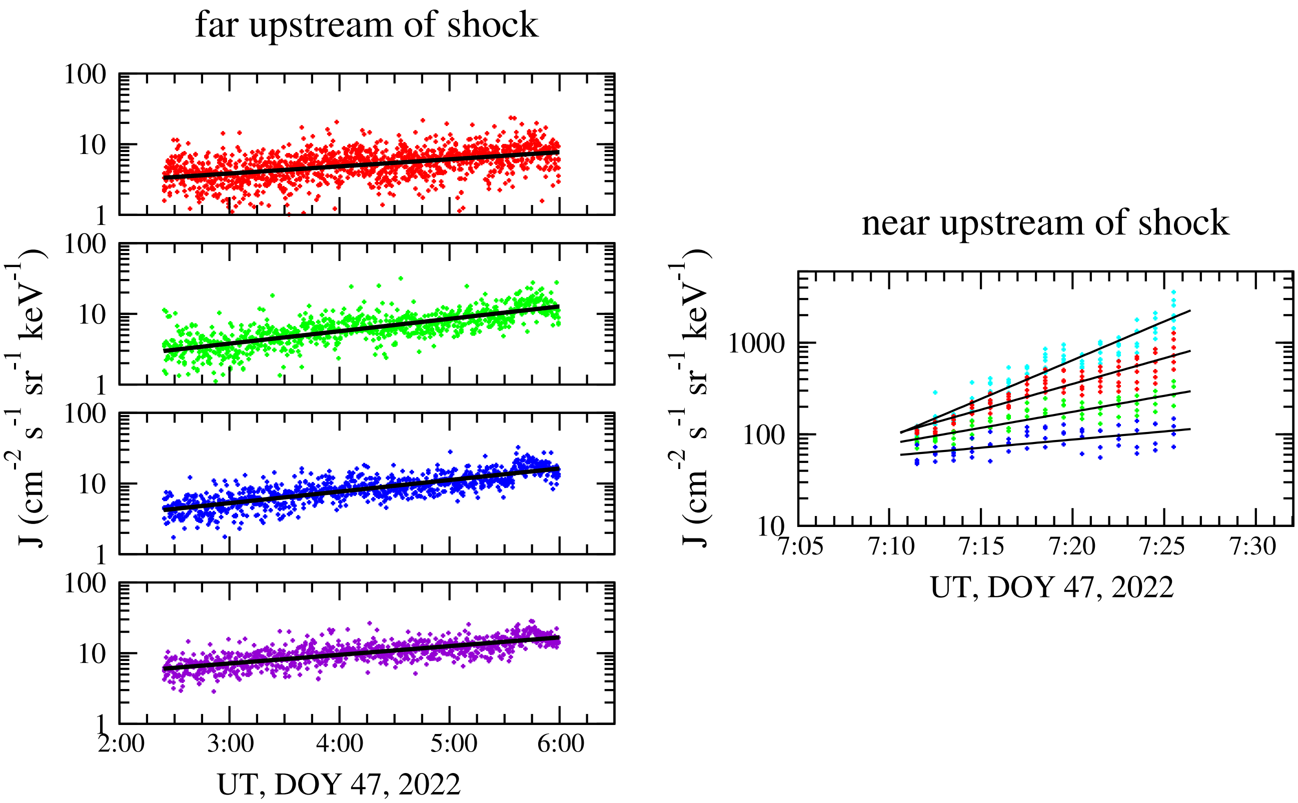

Figure 3. Differential intensity over selected intervals upstream of the shock: far from (left) and near the shock (right). The energies are: 75-keV (cyan), 133-keV (red), 237-keV (green), 421-keV (blue), and 750-keV (violet). The black lines in all panels represent the least-squares fit to the data, with the exponential rise time and correlation coefficient shown in Table 1.

coefficient, R_C. We do not show a profile for 75-keV protons far upstream of the shock, and for the cases near the shock, we do not show a profile for 750-keV protons. The reason is that we only show the results for the case of the largest correlation coefficients in the least-squares analyses, which, as it turns out, is $R_C > 0.47$.

The exponential rise time of the particle fluxes is related to the diffusion coefficient according to (see Eq. 7 of Giacalone 2012):

$$\kappa = W_1 V_{sh} \Delta t \tag{1}$$

where W_1 is the component of the plasma velocity normal to the shock, in the shock rest frame, and V_{sh} is the speed of the shock in the spacecraft frame. Assuming the shock is moving radially away from the Sun, then $W_1 = V_{sh} - U_1$, where U_1 is the radial component of the solar wind speed in the

Far Upstream				
E_{min}, E_{max}, E (keV)	Δt (hr.)	R_C	κ (cm^2/s)	$\lambda_{\parallel}$ (AU)
56.2, 100, 75	15	0.21	2.4×10^{20}	0.12
100, 178, 133	9.9	0.48	1.5×10^{20}	0.060
178, 316, 237	5.7	0.75	8.7×10^{19}	0.026
316, 562, 421	6.1	0.80	9.4×10^{19}	0.021
562, 1000, 750	8.1	0.74	1.3×10^{20}	0.021
Near Upstream				
E_{min}, E_{max}, E (keV)	Δt (min.)	R_C	κ (cm^2/s)	$\lambda_{\parallel}$ (AU)
56.2, 100, 75	12	0.94	3.0×10^{18}	1.6×10^{-3}
100, 178, 133	17	0.91	4.6×10^{18}	1.8×10^{-3}
178, 316, 237	29	0.87	7.3×10^{18}	2.2×10^{-3}
316, 562, 421	56	0.59	1.4×10^{19}	3.2×10^{-3}
562, 1000, 750	150	0.23	3.8×10^{19}	6.4×10^{-3}

Table 1. The top part of this panel refers to the time interval **2:30UT to 6:00UT on DOY 47**, far upstream of the shock, while the bottom portion is for the interval **7:11UT to 7:26UT on DOY 47**, near upstream of the shock. E_{min} and E_{max} define the energy range, and E is the logarithmic middle of the energy range. Δt is the exponential rise time associated with the intensity increase, determined by a least-squares fit to the data shown in Figure 3. Note that the units of Δt is hours for the case far upstream of the shock, and minutes in the near upstream time period. R_C refers to the correlation coefficient of the least-squares fit. The final column is the diffusion coefficient determined from Equation 1 using $W_1 = 532$ km/s, and $V_{sh} = 800$ km/s, respectively.

spacecraft frame. Estimating these quantities requires plasma data, which is shown a bit later, in Figure 7. It turns out that the plasma velocity and density vary considerably during this period, making it difficult to arrive at a good estimate of either. For W_1, we averaged the radial component of the observed solar-wind velocity from the time period **4:48UT 7:12UT on DOY 47**, giving a value $W_1 = 532$ km/s. The shock speed was estimated by assuming mass continuity across the shock. Using the observations of the plasma number density and radial speed for the four points prior to and after the shock crossing, we estimate the shock speed to be 800 km/s. We use this value for our estimate of κ based on Equation 1. The results are given in Table 1. As we discuss below, there is some evidence that the shock was decelerating at the time it crossed PSP, complicating the estimate of the shock speed. We also suggest a bit later that the shock may be consistent with that of a blast wave. If this is the case, our approach of using just the few data points in the vicinity of the shock seems to us to be the most reasonable. This is discussed further in Section 5.

The diffusion coefficient, κ, in this case is the component of the diffusion tensor along the radial direction, which we assumed was the direction of the unit-normal to the shock front. Judging from Figure 1, the magnetic field is nearly radial during this period (the radial component of the field is close to the magnitude throughout most of the interval), so that this diffusion coefficient is close to that along the magnetic field, or the so-called parallel diffusion coefficient. The parallel mean-free path is related to this according to, $\lambda_{\|} = 3\kappa/v$, where v is the particle speed. $\lambda_{\|}$ is given in the far right column in Table 1.

For comparison, have also used another method to determine diffusion coefficients using the observed magnetic field and quasi-linear theory (e.g. Jokipii 1966; Giacalone & Jokipii 1999). In this case, the spatial diffusion coefficient parallel to the mean magnetic field is determined from the pitch-angle diffusion coefficient that depends on the turbulent component of the magnetic field. For this case, we use Equations 12 and 13 of Li et al. (2022), and consider the n component of the magnetic field, which is transverse to the mean field direction. We consider the same time intervals as discussed above, which determines the longest temporal scale of the power spectrum. In both cases we use 9Hz (0.11s) resolution magnetic field, which determines the smallest temporal scale. As discussed in Li et al. (2022), a minimum pitch-cosine is needed for the required integration to relate the pitch-angle and spatial diffusion coefficients. This is because the observed magnetic power spectrum falls off sharply at high frequencies due to the dissipation of turbulence, and this has an important effect on the scattering of particles near ninety-degrees pitch angle. In our case, we use a value of 0.05 for the minimum pitch cosine. The results of this calculation are discussed below.

The estimated diffusion coefficients are shown graphically in Figure 4, with the black open-circle symbols representing the values far upstream of the shock, and the red open-circle symbols representing the values closer to the shock. **The solid lines in this figure are least-squares fits to these data. For the case of the far-upstream values, the diffusion coefficients are approximately independent of energy. For the near-upstream values, we find that the data is consistent with $\kappa_{rr} \propto E^{0.9}$. The dashed lines in this figure are the results from the calculation using the quasi-linear theory, as discussed in the preceding paragraph, with the colors corresponding to the same time intervals – far from the shock, or near the shock – for the data symbols and solid lines. For the interval near the shock, the estimates of κ from the two different methods are generally consistent; however, far from the shock, the estimate based on the quasi-linear theory is considerably smaller than that based on the exponential decay of the particle intensities. The two methods also do not give the same energy dependence. In fact, previous work has noted a similar discrepancy between predictions from quasi-linear theory using the observed magnetic field power spectrum and a separate compilation of diffusion coefficients determined from other methods (Palmer 1982; Bieber et al. 1994). It is worth noting that diffusion coefficients and mean-free paths determined from the exponential rise of the energetic-particle intensity near interplanetary shocks (e.g. Beeck & Sanderson 1989; Tan et al. 1989; Giacalone 2012; Wijsen et al. 2022) are smaller than those of the so-called Palmer consensus (Palmer 1982), and in this particular case, they also seasonably agree with the predictions of quasi-linear theory.**

The change in the energy dependence of the diffusion coefficient, **estimated using our first method discussed above,** is noteworthy, but not easy to interpret. The diffusion of charged particles is the result of scattering by magnetic irregularities (e.g. Jokipii 1966); thus, we might expect that there is a change in the behavior of the magnetic field far from the shock and near the shock. It is generally predicted that close to the shock, the higher intensity of energetic particles leads to the excitation of magnetic fluctuations which help trap the particles near the shock (e.g.

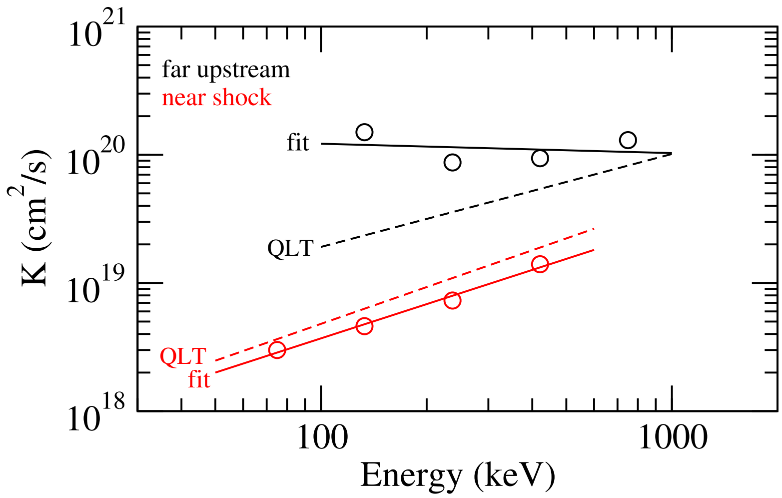

Figure 4. Open circle symbols are diffusion coefficients far upstream (black) and near the shock (red), estimated from the rise-time analysis, and tabulated in Table 1. The **solid** lines are least-squares fits to these data. **The dashed lines are estimates based on quasi-linear theory using the measured power spectrum of magnetic field fluctuations for each of these time intervals. See the text for more details.**

Bell 1978; Lee 1983). Such self-excited waves are sometimes seen at interplanetary shocks, but not always, or even often. **In this case, it is noteworthy that our estimates of the diffusion coefficients from quasi-linear theory are larger far from the shock than near the shock, suggesting enhanced magnetic fluctuations near the shock.** Later we show the magnetic field over a somewhat shorter time interval near the shock (Figure 7a). By inspection of this figure, it does seem that the magnetic field changes behavior close to the shock, which may account for the change in magnitude and energy-dependence of the diffusion coefficient. It is puzzling, however, that the diffusion coefficient far from the shock is independent of energy. Far from the shock, the magnetic field is that of the ambient solar wind and is presumably un-affected by the low-intensity of the energetic particles. Based on estimates of energetic-particle diffusion coefficients from quasi-linear theory using the well-observed power spectrum of interplanetary magnetic field fluctuations (e.g. Bieber et al. 1994; Giacalone & Jokipii 1999), the diffusion coefficient should be a function of energy. The discrepancy with our present analysis suggests that we do not well understand the energy dependence of the diffusion coefficient in interplanetary space (see also Palmer 1982).

3.2. *Determination of the Source of Accelerated Particles*

Inspection of Figure 1 reveals that this SEP event is characterized by a large increase in $\sim 0.05-2$ MeV proton intensities from a very low background. For instance, at 79.1 keV, the lowest energy shown in the middle panel of this figure, the peak intensity at the shock is more than 3 orders of magnitude larger than the intensity just after the event onset, and more than 4 orders of magnitude larger than the background fluxes between **18:00UT DOY 46 to 0:00 UT DOY 47**. These particles must come from an abundant source. The most likely candidate is that of the solar wind, as we show below.

It has been suggested that pre-existing suprathermal particles are an important source of SEP events, even those associated with fast CME-driven shocks. For instance Mason et al. (2006) noted a significant enhancement of 3He in large CME-related events, despite that 3He has a comparatively low abundance in the solar wind. These authors concluded that pre-existing high-energy 3He, which is often seen associated with small solar flares, is re-accelerated at CME-driven shocks, accounting for their observations. In addition, the standard theory of diffusive shock acceleration (DSA) only predicts that particles are accelerated from some lower energy, but does not address either the value of this low energy, or the source of the particles. In fact, the theory is based on the assumption the pitch-angle distribution is isotropic, and an analysis of this assumption at low energies (c.f. Giacalone 2003; Guo et al. 2021) suggests that the theory is only applicable at energies much larger than the energy of a proton moving at the speed of the shock. For this event, the shock speed was estimated in the previous section to be about 800 km/s, corresponding to a proton energy of about 3.4 keV. DSA theory can be applied to a pre-existing suprathermal particle distribution whose energies are considerably larger than a few keV, as was done by Guo et al. (2021) (see Sec. 3.3 of their paper). For the case in which the initial source spectrum with a corresponding phase-space density, $f_{ST}(p)$ having a power-law dependence on momentum, p, with a spectral index of δ, application of DSA theory gives the following for the phase-space density at, and downstream of the shock:

$$f_{sh} = f_{ST}(p_0)\frac{\delta}{\delta - \alpha}\Big[\Big(\frac{p}{p_0}\Big)^{-\alpha} - \Big(\frac{p}{p_0}\Big)^{-\delta}\Big] \tag{2}$$

where $\alpha = 3r/(r-1)$, r is the plasma density jump across the shock, and p_0 is the "injection" momentum, which can be related to the injection energy, E_0. As noted above, DSA theory is only strictly applicable for values of E_0 very much larger than a few keV. $f_{ST}(p_0)$ is the value of the phase-space distribution function for the pre-existing population of particles at the momentum p_0. This equation was derived in Guo et al. (2021) starting with an equation derived by Neergaard-Parker & Zank (2012).

In the limit $\alpha < \delta$, then at high values of p, the distribution is dominated by the first term, which is the standard result of DSA in that acceleration proceeds from a low-energy source leading to a power-law spectrum with a spectral index that depends only on the shock density compression ratio. In the limit $\delta < \alpha$, the distribution at the shock is dominated by the second term, which has the same spectrum as the source, but boosted in intensity by the factor $\alpha/(\alpha - \delta)$. If this limit applies, as it might for weak interplanetary shocks, we would expect the distribution of high-energy particles at the shock to have a similar spectrum, but slightly higher in intensity, to that of the pre-existing distribution, which may explain the observations of Desai et al. (2004).

For the 16 Feb 2022 event analyzed in this paper, we find that the spectrum at the shock has a power-law dependence on energy with a spectral index of about 1.6 (see Section 2.1). This corresponds to a power-law dependence of the phase-space density on momentum with an index of ~ 5.2. This is close to the quiet-time spectrum suggested by Fisk & Gloeckler (2006). Thus, it is reasonable to consider the special case that the downstream spectrum and pre-existing quiet-time spectrum have the same spectral index. Taking $\alpha = \delta$, it is straightforward to show: $f_{sh}/f_{ST} = \alpha \ln(p/p_0)$, where $f_{ST} = f_{ST}(p_0)(p/p_0)^{-\delta}$. This can readily be converted to differential intensity, giving

$$\frac{J_{sh}}{J_{ST}} = \ln \left(\frac{E}{E_0}\right)^{\gamma+1} \tag{3}$$

where J_{ST} is differential intensity spectrum of the pre-existing particles, and and γ is the power-law index associated with the energy spectrum ($\gamma = \alpha/2 - 1$).

To illustrate the application of this to determine whether the source of particles is a pre-existing suprathermal distribution, we consider the flux of protons with an energy of 174 keV. This choice is rather arbitrary, but illustrative. This energy is considerably higher than the lower-limit of applicability of DSA theory, which is well above the 3.4keV value noted above. The flux of 174 keV protons is shown as plus symbols in the top panel of Figure 5 along with three dashed lines. The blue dashed line in this figure refers to an approximate upper limit on the value of the "quiet time" flux at the energy of 174 keV. The actual value of the quiet time flux at this energy must be lower than this, at least during the nearly 1-day time period preceding the CME-related SEP event. We denote this as $J_{ST}(174$ keV). The red dashed line in this figure shows the prediction of J_{sh}, based on Equation 3, for the case in which the injection energy $E_0 = 2$ keV. We used $\gamma = 1.6$, which corresponds to the downstream spectral index as discussed in Section 2.1. The red dashed line is very much below the observed peak at the shock, which is represented as a black dashed line. In fact, the difference is about two orders of magnitude. Since this line is so much lower than the observed flux at the shock, this analysis effectively rules out a pre-existing high-energy population of protons, re-accelerated at the shock, as the source of particles for this event. Larger values of E_0 lead to even lower values of the predicted $J_{sh}(174\text{keV})$. Smaller values of E_0 will give somewhat larger values of the predicted flux at the shock, but, on the one hand, even values of a few eV give a predicted flux still far below what is observed; while, on the other hand, as noted above, such small values are already below those for which DSA theory is applicable.

The middle and bottom panels in Figure 5 are the same analysis repeated for helium and oxygen ions (using the ChanC data product), using approximately the same energy per nucleon for the observed fluxes, and the initial energies (E_0) in the analysis described for the protons. For example, for the case of helium, the range of total energies, shows as black symbols, are 637-723 keV, with a logarithmic middle energy of 678 keV, corresponding to 170 keV/nuc. The blue dashed lines in these two panels are upper bounds on the pre-existing tail, and are the values at the one-count level. If there is a pre-existing population of particles, its intensity is below these blue dashed lines. We repeat the same steps as we did for the protons. From the middle panel we see that the red dashed line, for the case of $E_0 = 8$ keV (2 keV/nuc.), which represents the expected value of the flux at the shock of shock-accelerated pre-existing particles, is well below the observed value shown in black. Thus, the source of helium ions in this event must come from a source other than a pre-existing high-energy tail, re-accelerated at the shock. The bottom panel shows the same analysis for oxygen ions, with a similar energy per nucleon as that of the protons and helium. This test is not as conclusive as that for the other two species given the rather limited statistics, but is still suggestive that the source of oxygen for this event is also not a re-accelerated pre-existing suprathermal distribution of particles.

The most likely source is the solar wind, which has a density that far exceeds that of the energetic protons. It has been shown in self-consistent plasma simulations of particle acceleration at shocks, such as the well-known hybrid simulation, that thermal plasma can be readily accelerated to high energies, for both quasi-parallel and quasi-perpendicular shocks (c.f. Ellison & Eichler 1984; Scholer 1990; Giacalone et al. 1992; Giacalone 2005). The injection process is related to the kinetic dissipation that maintains the collisionless shock. So-called "supercritical shocks", with Alfv́en Mach numbers larger than about 2.7 (e.g. Kennel et al. 1985), such as the event studied here, are known to require additional dissipation than that provided by resistivity between the electrons and ions in the shock layer (.e.g Leroy et al. 1981; Winske 1985). It is found that a fraction of the thermal ions incident on the shock are specularly reflected at the shock ramp, and return back upstream where they gyrate around the magnetic field and return to the shock and advect downstream of it. These ions are suprathermal in the frame moving with the upstream plasma. This process has been well observed at Earth's bow shock (e.g. Gosling et al. 1981). A fraction of these ions can be reflected again at the shock and are further energized, forming the high-energy tail on the distribution, as seen in the hybrid simulations referenced above. It is generally found that the energy flux contained in the high-energy tail can be as much as 10-20% of the dynamic energy flux incident on the shock (Giacalone et al. 1997).

In the bottom panel of Figure 6 we show the dynamic solar-wind energy flux, $(1/2)m_pnV^3$, as black circle symbols, and the enthalpy flux of 79-1600 keV ions, $5/2P_{ep}V$, as violet circle symbols, as a function of time for this event. P_{ep} is the partial pressure of the energetic ions, obtained from the observed energy spectrum (over the same energy range of 79-1600 keV), which is shown in the top panel in violet symbols. In these expressions, V is the component of the solar wind speed in

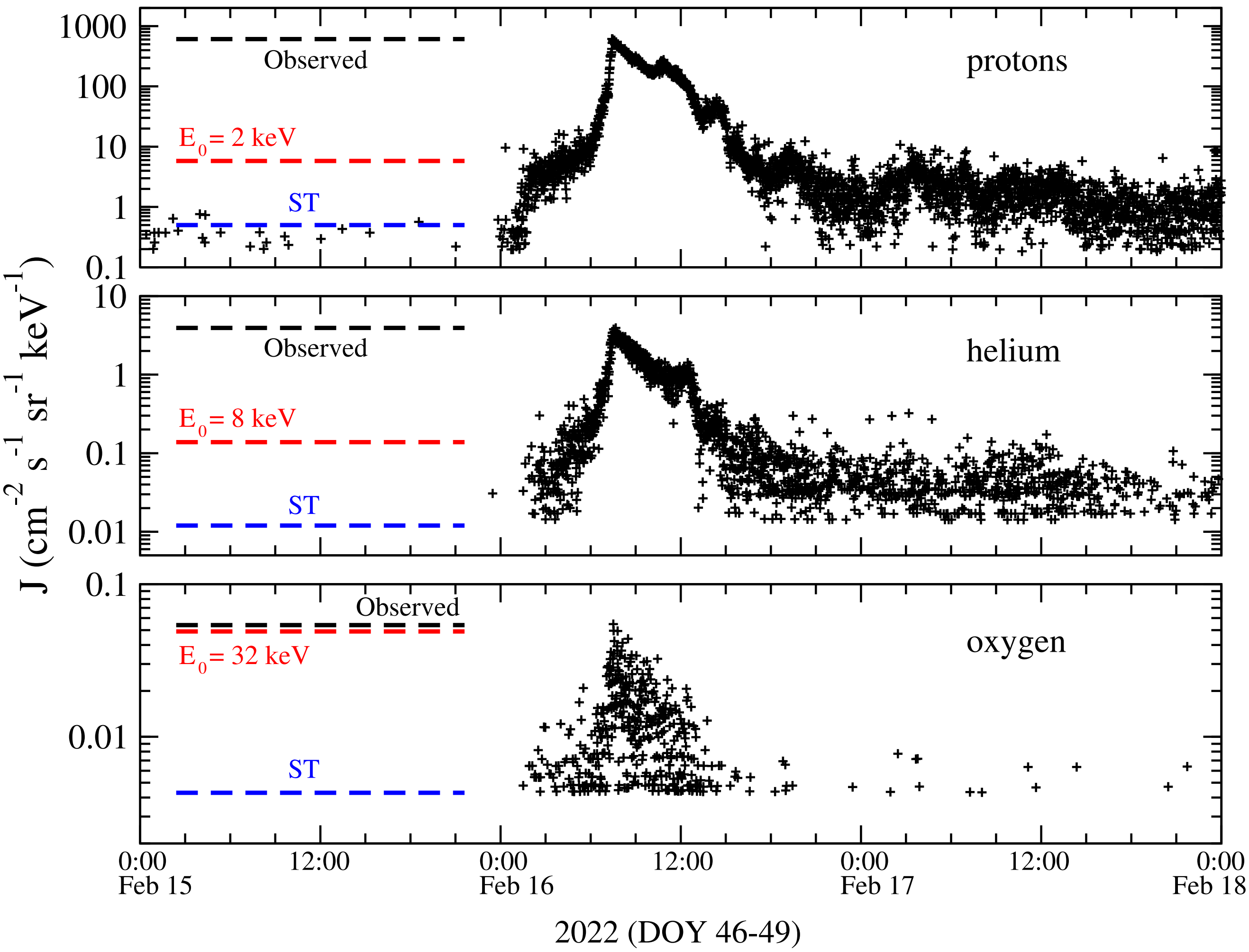

Figure 5. Top: (Black plus symbols) Flux of 165-184 keV protons (logarithmic-middle energy of 174 keV) for a 3-day period including the ESP event of 16 Feb 2022. (Blue dashed line) an approximate estimate of the upper bound on the pre-existing flux of particles within this energy range, for $\sim$ 1-day period prior to the initial increase. (red dashed line) the estimate of the increase of particles at the shock resulting from the acceleration of the pre-existing particles at the shock based on diffusive shock acceleration theory for an injection energy of 2 keV. (black dashed line) the value of the flux at the shock arrival. Middle and Bottom: Same format as the top panel, but for the case of helium (middle) and oxygen (bottom) ions with approximately the same energy per nucleon as the protons. For helium, the range of total kinetic energy is 637-723 keV: and for oxygen, it is: 2.38-2.73MeV. See text for more details.

the radial direction as measured in the shock frame, given by $V_{sh} - U_r$, where U_r is the measured spacecraft-frame radial solar wind speed, which was obtained from the SWEAP instrument. We

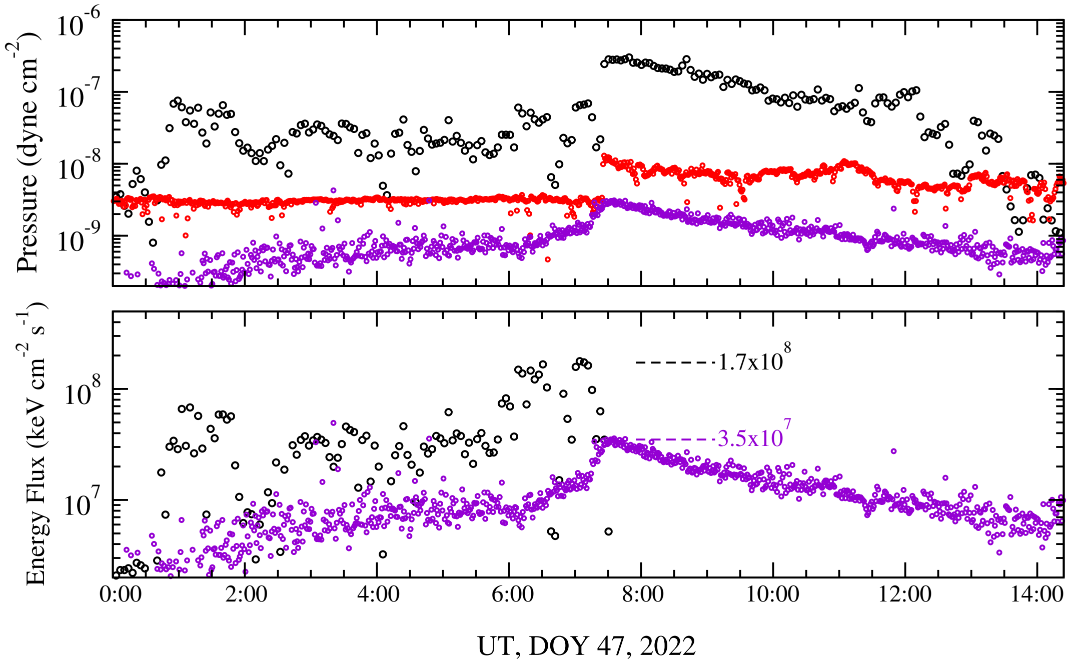

Figure 6. (Top panel) Partial pressures of SEPs (violet symbols), dynamic pressure of solar wind (black symbols), and magnetic field pressure (red symbols). (Bottom panel) Dynamic energy flux of the solar wind in the shock rest frame (black symbols), and the energetic-ion enthalpy flux (violet symbols). The dashed lines in the bottom panel show the values near the shock. See the text for more details.

assumed $V_{sh} = 800$ km/s for this analysis. We note that U_r exceeds the estimated shock speed behind the shock leading to a negative value of the dynamic energy flux downstream of the shock, and we did not plot these values since our vertical axis uses a logarithmic scale. Also shown in the top panel of this figure are the spacecraft-frame dynamic energy pressure, $nm_pU_r^2$ as black circles, and the magnetic pressure, determined from the observed magnitude of the field obtained from the FIELDS instrument, as red circles.

The two dashed lines shown in the bottom panel of Figure 6 show the values of the two plotted quantities at the shock. The ratio of the energetic-particle enthalpy flux (violet) to the dynamic solar-wind energy flux (black) is about $3.5/17 \approx 0.2$. This suggests that the shock converts about 20% of the incoming ramming energy flux into energetic particles, thereby providing an estimate of the acceleration efficiency. This is similar to that estimated in CME events by Mewaldt et al. (2005). We note that this estimate is very sensitive to the value of the shock speed.

We conclude from the above, that the source of energetic protons in this event is the solar wind. It is clear that the source is not a pre-existing suprathermal seed population. The solar wind has enough energy to account for the observed intensity of energetic ions, and there is a reasonable explanation on the physics of this process based from the results of previous self-consistent plasma kinetic simulations.

It is also important to emphasize that while we have suggested that the acceleration of solar-wind protons at the shock is related to the shock dissipation process, this is not necessarily true for minor ions. Minor ions have a negligible contribution to the energy budget of the plasma, field, and energetic particles. Thus, the injection of these ions into the shock acceleration process could well be different from that of the protons.

3.3. *The Decay Rate of Particle Intensity Behind the Shock*

The bottom panel (e) of Figure 7 shows fluxes of 79.1-keV to 1.66-MeV protons over a 9.6-hour period approximately centered on the arrival time of the shock, indicated with the vertical dashed line. The color coding of the ion fluxes are the same as that in Figure 1. The other panels show the plasma density (top, panel a), radial component of the solar-wind velocity vector (panel b), t- and n-components of the plasma velocity, in red and green, respectively (panel c), and the magnetic field vector and magnitude (panel d), with the same color coding as that shown in the top panel of Figure 1.

The energetic-proton fluxes peak at the shock and then decay downstream all at very nearly the same rate at all energies. The prediction of steady-state diffusive shock acceleration (DSA) theory for a planar shock is that the fluxes should be constant downstream. Thus, the observed behavior is not consistent with the prediction of the *standard* solution of DSA theory. This behavior has been noted previously in large ESP events (Reames et al. 1997; Daibog et al. 2000), and might be an example of the so-called "reservoir" phenomenon (e.g. Reames 2023; Dalla et al. 2002, and references therein). In most of the events studied previously, the intensity decay occurs over a considerably longer time scale than is seen in the 16 Feb 2022 event, and typically at higher energies than in this event. Moreover, this phenomenon is certainly not always observed, since there are other observations of ESP events, especially in the energy range we are interested in this event, which reveal nearly constant fluxes behind the shock (c.f. Giacalone (2012), and Figure 1a of Lario et al. (2018)). The more-rapid decay in the event studied here might be due to the fact that PSP is much closer to the Sun than 1au. If this is an example of the reservoir phenomenon, it is reasonable to expect the decay rate to be related to the rate at which the volume of the reservoir is increasing; and since it is closer to the Sun, the volume likely expands more rapidly leading to a higher rate of decay. Another possibility is that the decay is caused by diffusive transport away from the source. Since the observed decay rate is nearly the same at all energies, suggests that if this were the case, the diffusion coefficient must be independent of energy. This would lead to a very interesting scenario, given the results presented in Section 3.1, where the diffusion coefficient is independent of energy everywhere except for very near the shock.

It is also noteworthy, however, that the plasma density (top panel, a) also decreases approximately exponentially from the shock into the downstream region over roughly the same time period as the energetic-proton fluxes. This suggests that the decay in energetic particles might be related to the decay in plasma density. **On the one hand, as we showed in the previous section, the source of the accelerated particles is the solar wind; therefore, it seems entirely reasonable that the energetic particles and solar wind density are correlated. Although this is not as simple as it might otherwise seem since the energetic particles are more mobile than the solar wind and it is not immediately clear why they would have the same spatio-temporal behavior as the plasma. On the other hand, as we discuss in Secton 5, the decay in the plasma density is consistent with that expected from an over-expanding CME. In this case, the over-expansion leads to the energetic particles filling an increasing volume, leading to their decrease as well. This is discussed further below.**

Another possibility is that the near-exponential decay is caused by adiabatic cooling of the energetic particles in the expanding solar wind behind the shock. Energy change in charged particles occurs when the particles encounter compressions or rarefactions in the plasma. Acceleration occurs at compressions, such as shocks, but rarefactions cause energy loss. The Parker transport equation

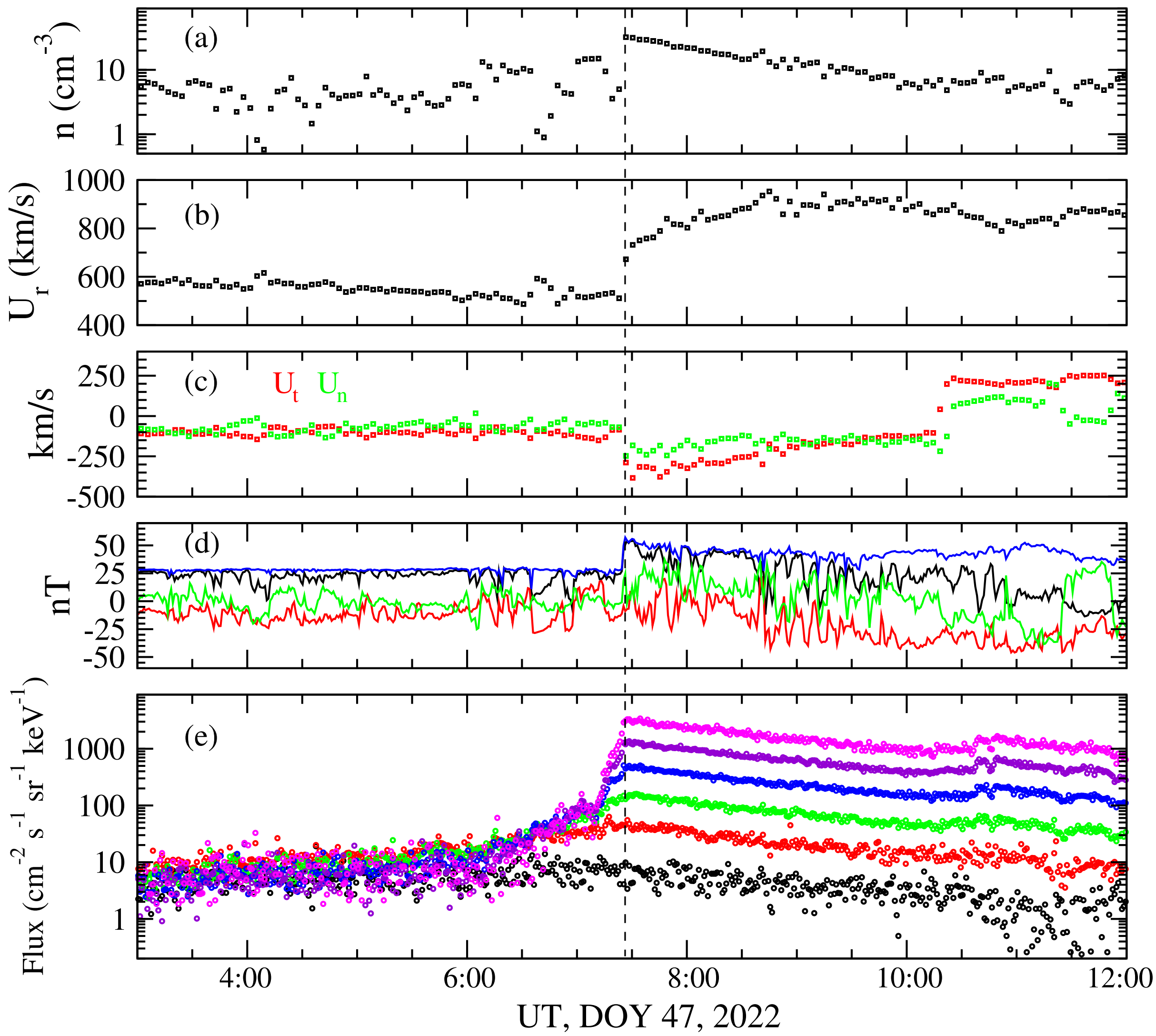

Figure 7. From the top panel, plasma number density, radial component of the solar-wind velocity, t- and $n-$ components of the solar wind velocity (red and green, respectively), magnetic field vector magnitude (black) and components (r, in blue, t in red, and n in green), and fluxes of 79.1 keV to 1.66 MeV energetic protons over a 9-hour period nearly centered at the shock crossing time, indicated with the vertical dashed line. The color code for the magnetic field and proton fluxes is the same as that shown in Figure 1.

(also known as the cosmic-ray transport equation) includes the energy term which is proportional to the divergence of the plasma velocity (e.g. Parker 1965). If we assume that downstream of the shock, this is the dominant term, we find:

$$\frac{\partial f}{\partial t} \approx \frac{1}{3} \nabla \cdot \mathbf{U} \frac{\partial f}{\partial \ln p} \tag{4}$$

where f is the phase-space distribution function, $\mathbf{U}$ is the plasma velocity vector, and p is the particle momentum. Assuming the distribution is a power law, consistent with the blue curve shown in Figure 2, it is readily found that this leads to:

$$\frac{1}{\tau_e} = \frac{\delta}{3}\nabla \cdot \mathbf{U} \tag{5}$$

where δ is the power-law index for the phase-space distribution function as a function of momentum. That is, $f \propto p^{\delta}$, and since the differential intensity is $p^2 f$, we find that $\delta = 2(1+\alpha)$, where α is the power-law index associated with the flux versus energy, as shown in Figure 2. For this case, we find $\alpha = 1.6$, giving $\delta = 5.2$.

By fitting the particle fluxes from the shock arrival time into the downstream region (later in time), we find that the e-folding time scale, $\tau_e \approx 2$ hrs. Thus, from Equation 5, we have: $\nabla \cdot \mathbf{U} \approx 0.29$ hr^{-1}. If assume that the plasma velocity is radial and nearly constant behind the shock (it clearly is not, as seen in Figure 7b, but this is addressed below), then $\nabla \cdot \mathbf{U} = 2U_r/r$, where r is heliocentric distance. PSP was located at $r = 0.35$ au at this time. With these assumptions, we find that that a value of $U_r \approx 2000$ km/s is required to account for the observed exponential decay, assuming it is caused strictly by adiabatic cooling in a uniform, radially expanding plasma. This value is considerably larger than the observed radial plasma speed shown in Figure 7b. Alternately, it is also instructive to consider that this cooling might be the result of a gradient in a direction other than radial. The middle panel (c) in Figure 7 shows the t and n components of the plasma flow for this event. One can clearly see a significant non-radial flow after the passage of the shock. Note that aside from the change in flow direction at the shock, there is another change in the flow direction at about DOY 47.43, which is real given that inspection of velocity distributions (not shown here) during this time period reveal that the solar wind was within the instruments field of view. If the divergence in the plasma velocity was dominated by the non-radial terms, for example the t direction, then we would have $\nabla \cdot \mathbf{U} \approx \Delta U_t / L_t$, where ΔU_t is the change in U_t over the length scale of variation in the t direction, represented by L_t. An upper limit on L_t would be, perhaps, half of the lateral extent of the CME, which is of the order of the heliocentric distance of PSP, 0.35AU, times half the CMEs angular extent. Based on a simulation of event discussed below, the angular extent appears to be of the order of, at most, 90-degrees, so that half of this is 45 degrees. This gives $L_t \sim 0.27$ au. Thus, setting the divergence of 0.29hr^{-1} equal to $\Delta U_t / L_t$, we obtain $\Delta U_t \sim 3250$ km/s. Judging from the red symbols in the middle panel of Figure 7c, the t component of the plasma speed does change slowly downstream, but the change is more than an order of magnitude smaller than this estimate. Thus, adiabatic cooling of energetic particles from the contribution to the plasma divergence arising from variations in the non-radial components of the plasma speed downstream of the CME shock cannot account for the observed exponential decay.

Adiabatic cooling may contribute to the decay in particle intensity behind the shock, however, based on the simple assumptions used above, it seems unlikely. We also do not favor the interpretation that this is caused by diffusive escape. This is likely related to previous examples of invariant spectra observed during the decay phase of large ESP events seen previously (e.g. Reames et al. 1997; Daibog et al. 2000; Dalla et al. 2002; Reames 2023). Yet, the behavior of the plasma density and velocity behind the shock are somewhat unusual, and, as we discuss below, suggest that the shock is undergoing a rather rapid change at the time it crossed PSP. In fact, as suggested by global modeling of the inner heliosphere at the time of the CME eruption, from the well-known ENLIL model (e.g. Odstrcil 2003), discussed below, PSP was very close to a large plasma compression associated with a co-rotating interaction region. This can be seen in Figure 8. We suggest below that this interaction led to the rapid, but probably short-lived deceleration of the CME-shock at about the same time it crossed PSP. Although this does not necessarily lead to a more-rapid adiabatic cooling of the high-energy particles that estimated above, it likely caused the reduction in plasma density behind the shock. Since the source of energetic protons is the solar wind, as we discussed in the preceding section, it seems reasonable that their fluxes are related to the plasma density.

As we now discuss, we suggest that the deceleration of the shock was caused by its interaction with an localized enhancement in plasma density, possibly related to a co-rotating interaction region. As the shock interacted with this density enhancement, it is reasonable that the flux of source particles was initially increased, but then, as the shock overtook the structure, the plasma density, and associated source particle flux, declined like the plasma density.

4. EVIDENCE OF A LOCALLY DECELERATING SHOCK

Consider the behavior of the radial component of the solar-wind velocity shown in Figure 8. There is a jump in the speed at the shock, as expected, but then the speed increases approximately linearly from about DOY 47.31 to DOY 47.36 before becoming approximately constant afterwards. In an idealized interplanetary shock, that is in steady state in the frame moving with the shock, mass conservation across the shock can be used to determine the shock speed. For a forward shock, if U_1 and U_2 are the observed solar wind speeds (normal to the shock, assumed to be radial), upstream and downstream of the shock, respectively, and n_1 and n_2 are the plasma densities upstream and downstream, then the shock speed is given by: $V_{sh} = (U_2 r - U_1)/(r-1)$, where $r = n_2/n_1$. For the ideal case, if we assume the shock is 'strong' in that the plasma density **jump** is nearly 4. **which is approximately consistent with that observed very near the shock**, then the shock speed is about $(4/3)U_2$. Thus, the behavior of the observed (approximately) linear increase in U_r immediately downstream of the shock shown in Figure 8 could be interpreted as the shock speed decreasing linearly. That is, if we take U_2 to be the observed speed after DOY 47.36, we obtain a shock speed of about 1000 km/s, which is larger than we have used in the analysis discussion in the previous sections, which is based on the properties of the shock seen locally at PSP. This suggests the shock is decelerating when it crossed PSP. Moreover, the decrease in density behind the shock would be expected if the shock crossed a larger density enhancement and then overtook it, and such an interaction would also likely cause the shock to slow down.

Figure 8 shows two images obtained from an ENLIL numerical simulation run[1], including a CME represented by the so-called "cone model", performed as a run-on-request from the Community Coordinated Modeling Center (CCMC). The two images are snapshots at the times given in the figure caption. The CME parameters used for this run on request were: lat=30, lon=-158, rad=51, vel=2554, and the CME was initiated on 22:09 UT on Feb 15, 2022. The images show plasma density times r^2, with the color code shown in the figure legends, in the equatorial plane. Also shown in

[1] https://ccmc.gsfc.nasa.gov/results/viewrun.php?domain=SH&runnumber=Joe_Giacalone_011623_SH_1

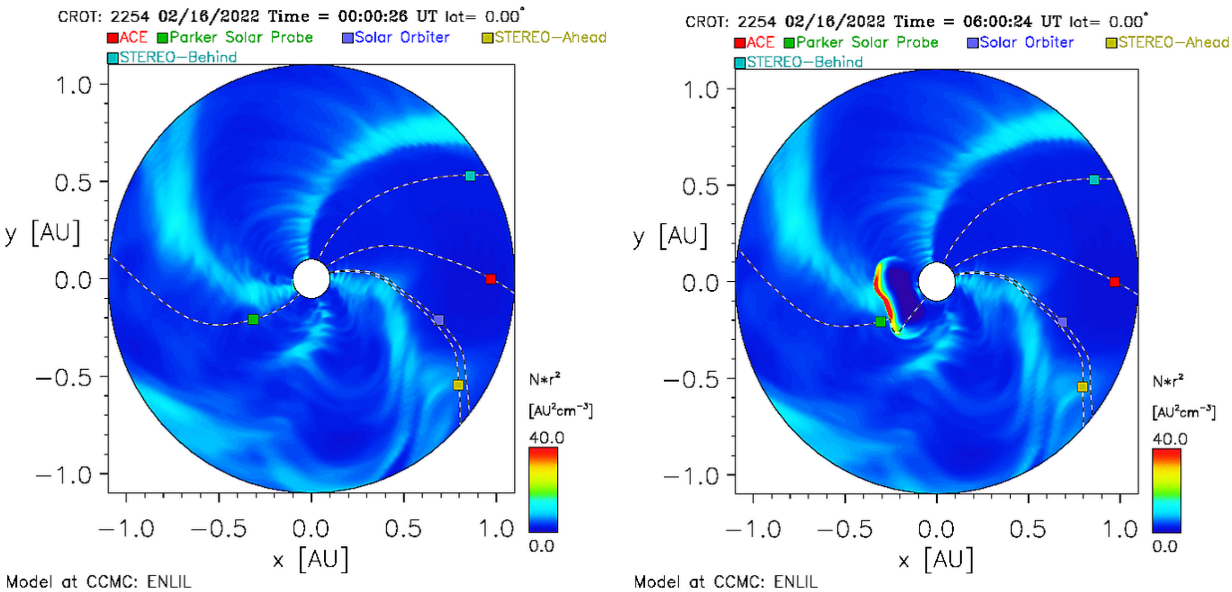

Figure 8. Results from the modeling of the solar wind in the inner heliosphere at about the time of the CME based on the ENLIL model (see text for details). Shown are two snapshots of the solar-wind density times r^2 in the ecliptic plane at two different times on 16 Feb 2022., as indicated above each image. The left image is for time=00:00:26UT, and the right image is for time=00:06:24, when the CME was just about the cross over PSP indicated with the green square in each image. Also shown are the positions of 5 spacecraft, as indicated above each image. The dashed lines are magnetic field that connect from the spacecraft to the inner boundary of the model calculation, at about 0.1 au.

these images are the positions of 4 spacecraft, as indicated above each image, as well as magnetic field lines which connect each spacecraft to the source surface at the center of the image.

The left image in Figure 8 shows the solar wind conditions just prior to the eruption of the CME and reveals a density enhancement associated with a corotating interaction region that is about to overtake PSP (the green square). The image at the right shows the time after the CME has launched and is just about to cross PSP. We see that the CME is also interacting with the pre-existing density enhancement at about the same time it crosses PSP. This is consistent with our suggestion above that the CME shock was decelerating locally as it crossed PSP.

The ENLIL simulation also provides plasma and field parameters at PSP as a function of time. In Figure 9, we show the results from this model run with the magnetic field field strength in black, plasma density in red, and radial plasma velocity in blue. The

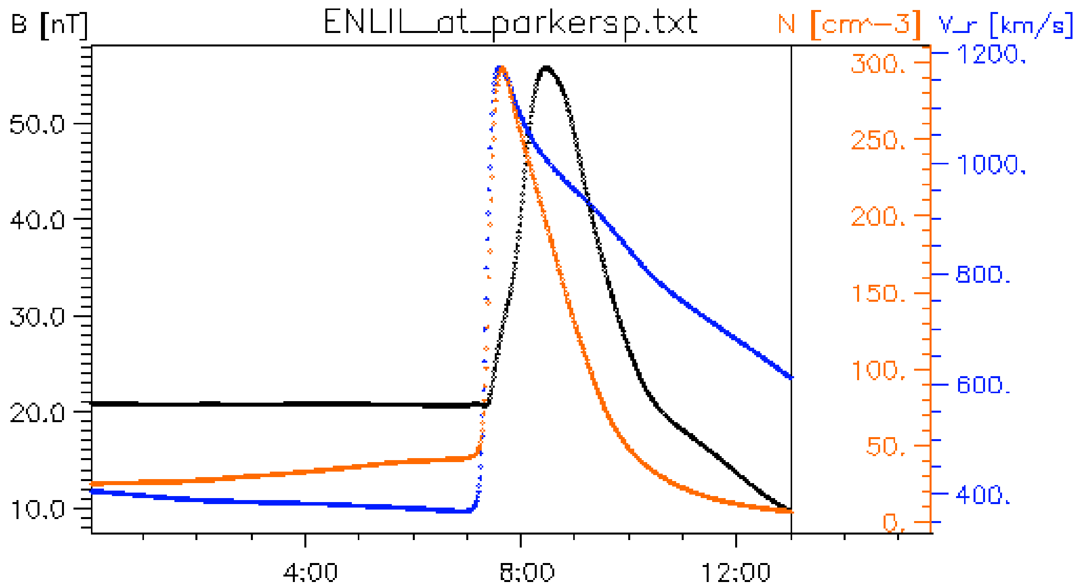

Figure 9. Magnetic field strength (black), plasma number density (red), and radial component of the solar wind speed (red) as a function of UT, DOY 47, 2022 from the ENLIL model of the 16 Feb 2022 CME at PSP.

model run provides a reasonable estimate of the arrival time of the shock, and the plasma density is qualitatively similar to the observed; however, the radial component of the flow velocity and the field strength time profiles do not agree with the observations after the passage of the shock. For instance, the ENLIL-model flow speed declines after the shock crossing, which is not consistent with that observed. This is perhaps not surprising given that this CME was on the back side of the Sun relative to the Earth, and the inner boundary conditions used in the model are not well constrained during this time period. Although these particular simulations do not demonstrate that the shock was locally decelerating, we show in the next section that such behavior is to be expected when a shock passes over a pre-existing density enhancement.

4.1. *Results from a One-Dimensional Hydrodynamic Simulation*

To test the rather simplified physics argument given above, we have performed a one-dimensional spherically symmetric hydrodynamic numerical simulation of a fast forward shock wave overtaking a pre-existing density structure. The details of this simulation are given in the appendix. In this section, we just present the results and interpretation. **It is important to emphasize that this numerical simulation is not a direct simulation of the 16 Feb 2022 CME, but, rather, a proof-of-concept to support our suggestion that a shock will undergo a deceleration as it crosses a pre-existing density enhancement, and that the resulting behavior of the density and flow speed are qualitative similar to that observed for this event. The parameters used in the one-dimensional simulation, however, are not based on observed values during the time period of the CME event.**

Shown in Figure 10 are simulated profiles of the plasma number density and solar wind speed (assumed radial) as a function of heliocentric distance at four different times, as indicated. The black curve are the profiles at 0.83 hrs after the start of the simulation. The top panel shows the pre-existing density enhancement at about 0.16 au. The fast disturbance is at about 0.1 au at this time and has already formed a forward/reverse shock pair. This is expected in the ideal case modeled here, even close to the Sun, in which a high speed radial flow overtakes a slow speed radial flow, since this model is spherically symmetric. At 3.19 hrs (red curves), the density enhancement is moved outwards and has also formed a forward/reverse shock pair. The reverse shock is located about 0.175 au, while the fast forward shock associated with the disturbance is approaching it at about 0.15 au. At 5.56 hrs (blue curves), the fast-forward shock of the disturbance has overtaken the reverse shock caused by the initial density enhancement. The density profile at this time shows a large density jump at about 0.2AU, which is caused by the forward shock overtaking the density enhancement of the reverse shock. At about 7.92 hrs (magenta curves), the fast forward shock, associated with the large disturbance (consider it the simulated CME), has overtaken the reverse shock completely and will later also overtake the forward shock seen at about 0.28 au.

Figure 11 shows the same profiles, but as functions of time as seen by three observers located at about 0.2 au, as indicated. These observers are located near the large density enhancement seen in the blue curve of the top panel of Figure 10. We note that there is a qualitative consistency between these time profiles and those observed for the PSP event described above, as can be judged by

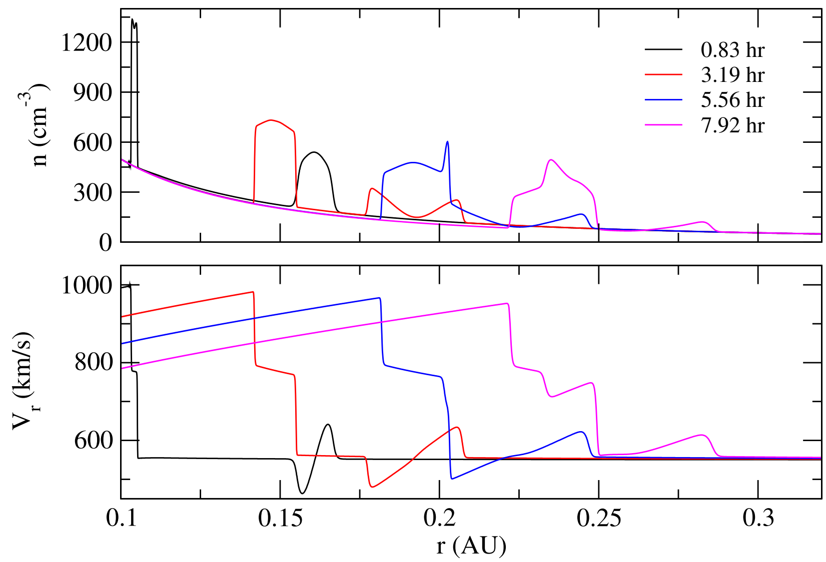

Figure 10. Fluid speed and density as a function of radial distance at 4 different times from a one-dimensional, spherically symmetric hydrodynamic simulation of a fast disturbance overtaking a pre-existing density enhancement. The times associated with each curve are indicated in the legend in the upper panel. See the text and the appendix for more details.

comparing the red curves of Figure 11 and the black circle symbols of Figure 7a-b. There are certainly quantitative differences between the results of our simulation and those observed. For instance, the density decrease behind the shock is not obviously exponential and does not decrease by as large a factor as that observed. Moreover, the increase in the flow speed from near the shock to further downstream is not obviously linear. And, the time scale of the variations are considerably smaller in the simulations compared to the observations. Regardless, the simulation is qualitatively consistent with the observations and is with our suggestion that the CME-driven shock was decelerated by its interaction with a pre-existing density enhancement. In this case, that structure was a co-rotating interaction region, as evidenced by Figure 8.

While we have provided evidence that the shock was decelerating locally as it crossed PSP, this does not obviously relate to the uniform decay of the energetic particles behind the shock, as discussed in Section 3.3. The cause of this remains unclear. In the next section, we discuss another possibility: the shock seen locally at PSP was caused by an over-expanding CME, leading to a blast wave. In

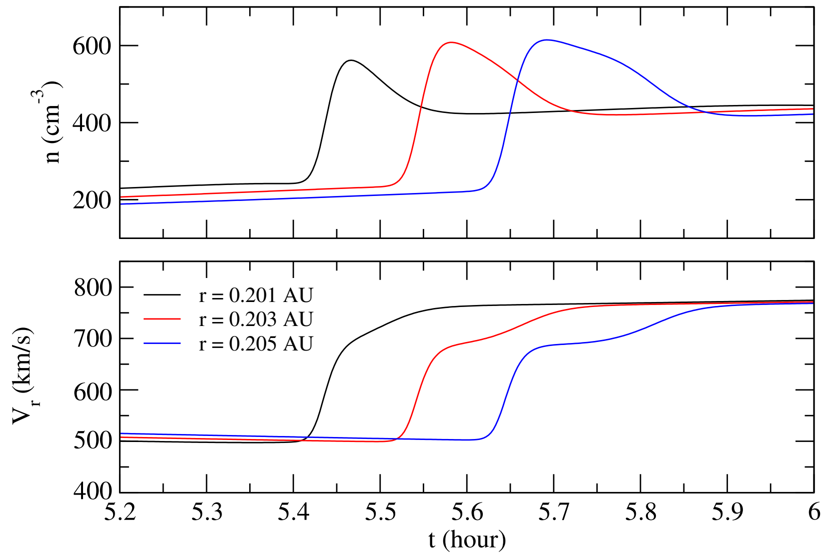

Figure 11. Same as Figure 9 except that these are profiles as a function of time seen by three different radial distances (observation locations) as indicated by the legend in the bottom panel. See the text for more details.

this scenario, the depletion of the SEPs behind the shock is caused by the energetic particles filling an increasing volume.

5. EVIDENCE OF A BLAST WAVE

As noted previously, the decay of energetic particles behind the shock is similar to the decay of the plasma density behind the shock. This behavior is expected if the shock were locally a blast wave, since it is well known that such shocks are associated with a region of over-pressure, followed by a significant decrease in the pressure (and density). A blast wave can result from a CME when its internal pressure is greater than that of the surrounding solar wind. Gosling et al. (1998) studied a few such cases observed by *Ulysses*. The CME in our case was directed towards a higher latitude than where PSP was located (Mierla et al. 2022), yet PSP observed a rather strong shock at its location. The enhancement in density and change in flow speed were rather large, despite that PSP was well south of the CME "nose".

We might reasonably assume that the radius of the blast wave is of the order of the distance between PSP and the Sun, which was about 0.35AU. In the well-known Sedov blast wave solution, it is found that after the initial increase in the plasma density (or pressure) at the shock, the density decays over a scale that is about 10% of the shock radius (c.f. Chapter 17 of Shu 1992). This gives a scale of the density variation for our case of about 0.035 au. Assuming the shock is moving 800 km/s, based on our previous estimate, it would take about 1.8 hours for such a scale to pass by PSP. This corresponds to about 0.07 of a day, and judging from Figure 7, this is consistent with the scale of the variation of the density and SEP intensity decays behind the shock. This rather simple estimate could be refined, and even include the speed of the spacecraft. However, our estimate is sufficient to justify the principal conclusion given that, at this time, PSP had a radial speed of less than 30 km/s, which is well below the $\sim$ 800 km/s speed of the shock.

Thus, we suggest that the SEP intensity increase behind the shock is the result of the SEPs filling an expanding volume associated with the propagation of a blast wave as it crossed PSP. We suggest that this is an example of an over-expanding CME, whose internal pressure is larger than that of the surrounding medium, and has been seen previously at larger heliocentric distances (e.g. Gosling et al. 1998). In this case, the over-expansion can drive shocks, or compressions that steepen into shocks farther from the Sun. However, the case analyzed here is much closer to the Sun and may indicate that over-expanding CMEs, a very explosive phenomenon, are more common closer to the Sun than previously realized. This interpretation may also explain why the rate of decay in the particle intensities for this event is shorter than seen in previous ESP events, as we discussed in Section 3.3.

6. SUMMARY AND CONCLUSIONS

We have presented a number of analyses of the CME-related ESP event observed by PSP on 16 Feb 2022 when the spacecraft was 0.35AU from the Sun. This event was broadly characterized as a significant enhancement in the intensity of $\sim$ 0.05-5 MeV protons, which started with a slow and gradual increase after the onset of a CME as seen by the STEREO-A Cor2 coronograph, peaking at the arrival of a shock, and then decayed significantly at the arrival of the ICME-flux rope. There were counts detected for this event up to 80 MeV/nuc, although our focus in this study was the ESP phase of the event at lower energies. The event began approximately 1.5 hours after a clear signature of the CME was seen in the STA/Cor2 images. The shock, and associated peak in energetic particles, occurred about 9 hours after the CME eruption. The ICME arrival occurred about 8 hours after the arrival of the shock.

Shortly after the onset of the ESP event, the fluxes of protons from $\sim$ 0.079-1MeV showed equal intensities lasting for 4-5 hours prior to the shock arrival. This represented a quasi-flat energy spectrum. While this feature has been noted in prior CME-related SEP events observed at 1 au (e.g. Lario et al. 2018), here we report this observation for PSP at 0.35 au. The fluxes during this period rose slightly with time until about 30-45 minutes prior to the shock where the fluxes began to rise more abruptly and with a rate that depended on energy such that the fluxes "separated". The spectrum at the shock from $\sim 0.079 - 1$ MeV had a power-law dependence on energy with a spectral slope of about -1.6. At higher energies, the spectrum was a bit steeper but also had a power-law dependence on energy.

We calculated diffusion coefficients by fitting the rate of increase of the proton fluxes both far from the shock, during the flat-spectra period, and closer to the shock, to exponential functions, representing diffusive decay in the intensity of particles with distance from the shock upstream. We found that far from the shock, the diffusion coefficient was independent of energy with a value of (0.87-1.5)$\times 10^{20}$ cm^2/s. Because the magnetic field was nearly radially outward during this time, this represents the parallel diffusion coefficient. For the period closer to the shock, we found that the diffusion coefficient increased with energy such that $\kappa_{rr} \propto E^{0.9}$, having a value of 3×10^{18} cm^2/s at the energy of 56.2 keV.

We also performed an analysis to determine the source of the energetic particles in this event, particularly on whether they could be produced by the enhancement of a pre-existing suprathermal population by re-acceleration at the shock. We did this by invoking diffusive shock acceleration theory for the case of a source of pre-existing particles having a high-energy power law dependence on energy and determined the increase in intensity of the re-accelerated particles at the shock. We constrained the intensity of the pre-existing high-energy particles by using the quiet-time intensity of particles with energies between 165-184 keV/nuc. We determined the intensity enhancement at the shock as expected from DSA theory and compared this to the observed increase for protons, helium, and oxygen. We found that the enhancement of the quiet time tail cannot account for the peak flux at the shock for protons and helium, while the test was not conclusive for oxygen. In fact, the peak flux of protons at the shock was some 3 orders of magnitude larger than the (upper bound) of the flux of quiet-time protons. For helium, the observed flux at this energy was some 2.5 orders of magnitude above the one-count level, which was used because there were no counts of quiet-time particles detected. For oxygen, the statistics were even more limited, and the peak at the shock was only a factor of 10 or so above the one-count level. The maximum enhancement, according to the theory, is only an order of magnitude, or less. We further showed that the energy flux contained in the energetic particles at the time of the shock crossing was about 20% of the incoming dynamic energy flux of the solar wind. Thus, there is sufficient energy in the solar wind to draw from to produce the energetic protons. We noted that the 20% value is consistent with previous self-consistent numerical simulations. We conclude that the energetic protons in this ESP event are the result of the acceleration of solar wind protons directly at the shock front. Our results also suggest that helium is also accelerated directly from the solar wind. This may also be true of oxygen, but our analysis was unable to make a definitive statement on this due to the limited statistics available.

This ESP event is also characterized by a near-exponential decrease in intensity of the particles immediately after the passage of the shock lasting for about an hour. We considered whether adiabatic cooling, caused by the divergence in the solar wind velocity vector downstream of the shock could account for this behavior. From the observations, we determined the e-folding decrease in the flux to be $\tau_e \approx 2$ hrs., which we assumed was the rate of cooling. We equated this time to that predicted from energetic-particle transport theory which relates the cooling rate to the power-law spectral index of the SEP energy spectrum and the divergence of the plasma velocity. From this, we estimated that to achieve the observed rate of flux decrease, the plasma would have to have a speed of 2000 km/s, which is far greater than that observed. Thus, this could not be caused by adiabatic cooling in a purely radial and constant shocked solar wind. We also considered whether variations in the non-radial directions might lead to a faster cooling rate, but this analysis was inconclusive.

We also noted that the observed solar-wind plasma density also decays behind the shock with same rate as that of the energetic particles. This suggests a close relationship between the two. As we have already concluded that the main source of energetic particles in this event is direct acceleration of thermal solar wind at the shock, it is perhaps not surprising that the time behavior of the two are related. The solar-wind velocity also had a time behavior that suggested the shock was undergoing, or had recently undergone, a deceleration. The global solar wind at this time, according to a ENLIL simulation, revealed that the CME occurred at a time where PSP was about to encounter a pre-existing plasma compression associated with a corotating interaction region. Therefore, the CME crossed over this compression, which, we suggest, caused the CME shock to slow down. To verify this, we performed a simple one-dimensional, spherically symmetric, hydrodynamic calculation of our own. We found that if an observer were to be fortuitously positioned as a shock wave overtook a large density enhancement, it would observe a time evolution of the density and radial flow speed that is qualitatively consistent with that observed by PSP in the 2022 Feb 15 event.

Finally, we also considered the possibility that the time behavior of both the plasma density and the SEPs behind the shock could be understood in terms of the passage of a blast wave across PSP. It has been noted previously that CMEs are an explosive-like phenomenon and can expand rapidly into the pre-existing medium, and lead to the existence of blast waves (Gosling et al. 1998). STA/Cor2 images of the CME in the event showed that the CME was propagating at a higher latitude than where PSP was located, yet PSP still observed the shock. If the shock seen by PSP was similar to that of a blast wave, then the plasma density would decrease approximately exponentially behind the blast wave, in the shocked plasma. The same is true of the energetic particles. This is an attractive possibility and, as PSP was located at some 0.35AU from the Sun at this time, may indicate that CME blast waves could be common close to the Sun.

This project was supported by the IS⊙IS instrument suite on NASA's Parker Solar Probe Mission, contract NNN06AA01C. Parker Solar Probe was designed, built, and is now operated by the Johns Hopkins Applied Physics Laboratory as part of NASA's Living with a Star program. Support from the LWS management and technical team has played a critical role in the success of the Parker Solar Probe mission. JG also acknowledges support from the NSF/AGS under grant 1931252, and NASA under grants 80NSSC20K1283, 80NSSC18K1213, and 80NSSC21K0119.

APPENDIX

Here we provide details of the hydrodynamic model presented in Section 4. We solve the equations presenting conservation of mass, momentum, and energy of a plasma with a mass density, ρ, fluid speed U, and thermal pressure P, in spherical coordinates, assuming a monotonic gas (ratio of specific heats of 5/3), given by:

$$\frac{\partial \rho}{\partial t} + \frac{1}{r^2}\frac{\partial}{\partial r}[r^2 \rho U] = 0 \tag{1}$$

$$\frac{\partial}{\partial t}(\rho U) + \frac{1}{r^2}\frac{\partial}{\partial r}\left[r^2\left(\rho U^2 + \nu_{art}\right)\right] + \frac{\partial P}{\partial r} = 0 \tag{2}$$

$$\frac{\partial}{\partial t}\left(\frac{1}{2}\rho U^2 + \frac{3}{2}P\right) + \frac{1}{r^2}\frac{\partial}{\partial r}\left[r^2\left(\frac{1}{2}\rho U^2 + \frac{5}{2}P + \nu_{art}\right)U\right] = 0 \tag{3}$$

These equations represent the time rate of change of the mass, momentum, and energy in terms of the divergence of the mass, momentum, and energy flux. We have included an "artificial" viscosity, ν in these equations in order to resolve shocks, and to force their widths to be of the same order as the grid spacing, which is important to our application. The viscosity is given by:

$$\nu_{art} = -C(\Delta r)^2 \rho \frac{\partial U}{\partial r}\left|\frac{\partial U}{\partial r}\right| \tag{4}$$

where C is a constant, which we take to be 2. In this expression, Δr is the distance between subsequent grid points, which is a function of r in our case since we use a logarithmic scaling of grid points in r. This form of the artificial viscosity has the effect of forcing the shock thickness to be a few grid cells (c.f. Potter 1980). Because of the $(\Delta r)^2$ factor, this term is generally very small except for very near a shock where gradient in the flow speed is the largest, and does not much effect the solution on scales larger than the shock thickness.

Note that we have neglected the magnetic field in this case for simplicity since our simulation is only meant to illustrate the basic physics of the interaction between a fast shock with a pre-existing density enhancement and is not meant to be directly compared with the observations.

Equations 1 - 4 are solved numerically using a high-order predictor-corrector method (third-order accurate in time, in this case). The predictor-corrector method is well known. The basic idea of this method involves an initial implicit time step to advance the fluid quantities (the terms inside the time derivatives) based on an evaluation of the necessary quantities (the other terms, involving spatial derivatives) at the current time step. This gives an estimate of the "predicted" quantities. This time step is then repeated using the predicted quantities. Spatial derivatives are computed using a 4th-order accurate spline method (c.f Press et al. 1986). We have tested this approach for accuracy by comparing with known solutions, such as expectations based on the shock-jump conditions, and find our solution to be accurate.

As noted above, we have chosen a spatial grid such that subsequent spatial locations are spaced equally in logarithm, giving, $\Delta r/r$ is a constant. Our grid consists of 25000 points, over the range 0.098AU $< r <$ 1.4AU. The time step is taken to be 0.02 seconds. The simulation is terminated after 9.6 hours. We consider the following initial conditions: the flow speed is taken to be constant with a speed 550 km/s. The number density is taken to fall off as $1/r^2$ with a value of 5 cm^{-3} at 1AU, and the thermal pressure is also taken to fall of as $1/r^2$ with a temperature of 1.9MK at the inner boundary. The variation of the pressure was taken rather arbitrarily, but given that the thermal pressure is smaller than the plasma dynamic pressure, our choice of the pressure does not much effect the general conclusions of our study.

At $t = 0$ a Gaussian-shaped density enhancement, with a width of 2.5×10^{-3} AU, and peak value at $r = 0.15$ AU is initiated. This enhancement evolves with time, forming forward and reverse shocks at either edge. This can be seen in Figure 9. At $t = 0.5$ hrs, a large impulse is created by setting the inner boundary to have a speed of 10^8 cm/s. The speed at the inner boundary after the release of this impulsive "blob" slowly decays exponentially over a scale of about 60 hours, which is far greater than the maximum simulation time. The result of this inner boundary condition is a fast moving compression which forms a forward/reverse shock pair, which both move outward relative to the Sun. This can also be seen in Figure 9.

REFERENCES

Bale, S. D., Goetz, K., Harvey, P. R., et al. 2016, SSRv, 204, 49, doi: 10.1007/s11214-016-0244-5

Beeck, J., & Sanderson, T. R. 1989, J. Geophys. Res., 94, 8769, doi: 10.1029/JA094iA07p08769

Bell, A. R. 1978, Mon. Not. R. Atron. Soc., 182, 147

Bieber, J. W., Matthaeus, W. H., Smith, C. W., et al. 1994, Astrophys. J., 420, 294, doi: 10.1086/173559

Bryant, D. A., Cline, T. L., Desai, U. D., & McDonald, F. B. 1962, J. Geophys. Res., 67, 4983, doi: 10.1029/JZ067i013p04983

Cohen, C. M. S., Christian, E. R., Cummings, A. C., et al. 2021, A&A, 656, A29, doi: 10.1051/0004-6361/202140967

Daibog, E. I., Stolpovskii, V. G., Svertilov, S. I., et al. 2000, Advances in Space Research, 26, 871, doi: 10.1016/S0273-1177(00)00021-1

Dalla, S., Balogh, A., Heber, B., Lopate, C., & McKibben, R. B. 2002, Journal of Geophysical Research (Space Physics), 107, 1370, doi: 10.1029/2001JA009155

Desai, M. I., Mason, G. M., Wiedenbeck, M. E., et al. 2004, ApJ, 611, 1156, doi: 10.1086/422211

Ellison, D. C., & Eichler, D. 1984, ApJ, 286, 691, doi: 10.1086/162644

Fisk, L. A., & Gloeckler, G. 2006, Astrophys. J., 640, L79, doi: 10.1086/503293

Fox, N. J., Velli, M. C., Bale, S. D., et al. 2016, SSRv, 204, 7, doi: 10.1007/s11214-015-0211-6

Giacalone, J. 2003, Planet. Space Sci., 51, 659, doi: 10.1016/S0032-0633(03)00101-6

—. 2005, Astrophys. J., 628, L37, doi: 10.1086/432510

—. 2012, Astrophys. J., 761, article id. 28, doi: 10.1088/0004-637X/761/1/28

Giacalone, J., Burgess, D., Schwartz, S. J., & Ellison, D. C. 1992, Geophys. Res. Lett., 19, 433, doi: 10.1029/92GL00379

Giacalone, J., Burgess, D., Schwartz, S. J., Ellison, D. C., & Bennett, L. 1997, J. Geophys. Res., 102, 19789, doi: 10.1029/97JA01529

Giacalone, J., & Jokipii, J. R. 1999, ApJ, 520, 204, doi: 10.1086/307452

Giacalone, J., Mitchell, D. G., Allen, R. C., et al. 2020, ApJS, 246, 29, doi: 10.3847/1538-4365/ab5221

Giacalone, J., Burgess, D., Bale, S. D., et al. 2021, ApJ, 921, 102, doi: 10.3847/1538-4357/ac1ce1

Gloeckler, G., Ipavich, F. M., Klecker, B., Hovestadt, D., & Scholer, M. 1985, in International Cosmic Ray Conference, Vol. 4, 19th International Cosmic Ray Conference (ICRC19), Volume 4, 182

Gosling, J. T. 1993, J. Geophys. Res., 98, 18937, doi: 10.1029/93JA01896

Gosling, J. T., Asbridge, J. R., Bame, S. J., et al. 1981, J. Geophys. Res., 86, 547, doi: 10.1029/JA086iA02p00547

Gosling, J. T., Riley, P., McComas, D. J., & Pizzo, V. J. 1998, J. Geophys. Res., 103, 1941, doi: 10.1029/97JA01304

Guo, F., Giacalone, J., & Zhao, L. 2021, Frontiers in Astronomy and Space Sciences, 8, 27, doi: 10.3389/fspas.2021.644354

Hill, M. E., Mitchell, D. G., Andrews, G. B., et al. 2017, Journal of Geophysical Research (Space Physics), 122, 1513, doi: 10.1002/2016JA022614

Jokipii, J. R. 1966, Astrophys. J., 146, 480, doi: 10.1086/148912

Kasper, J. C., Abiad, R., Austin, G., et al. 2016, SSRv, 204, 131, doi: 10.1007/s11214-015-0206-3

Kennel, C. F., Edmiston, J. P., & Hada, T. 1985, Washington DC American Geophysical Union Geophysical Monograph Series, 34, 1, doi: 10.1029/GM034p0001

Lario, D., Berger, L., Decker, R. B., et al. 2019, AJ, 158, 12, doi: 10.3847/1538-3881/ab1e49

Lario, D., Berger, L., Wilson, L. B., I., et al. 2018, in Journal of Physics Conference Series, Vol. 1100, Journal of Physics Conference Series, 012014, doi: 10.1088/1742-6596/1100/1/012014

Lario, D., Richardson, I. G., Palmerio, E., et al. 2021, ApJ, 920, 123, doi: 10.3847/1538-4357/ac157f

Lee, M. A. 1983, J. Geophys. Res., 88, 6109, doi: 10.1029/JA088iA08p06109

Leroy, M. M., Goodrich, C. C., Winske, D., Wu, C. S., & Papadopoulos, K. 1981, Geophys. Res. Lett., 8, 1269, doi: 10.1029/GL008i012p01269

Li, J.-T., Beacom, J. F., & Peter, A. H. G. 2022, ApJ, 937, 27, doi: 10.3847/1538-4357/ac8cf3

Mason, G. M., Desai, M. I., Cohen, C. M. S., et al. 2006, Astrophysical Journal, 647, L65, doi: 10.1086/507469

McComas, D. J., Alexander, N., Angold, N., et al. 2016, SSRv, 204, 187, doi: 10.1007/s11214-014-0059-1

McComas, D. J., Christian, E. R., Cohen, C. M. S., et al. 2019, Nature, 576, 223, doi: 10.1038/s41586-019-1811-1

Mewaldt, R. A., Cohen, C. M. S., Labrador, A. W., et al. 2005, Journal of Geophysical Research (Space Physics), 110, 9, doi: 10.1029/2005JA011038

Mierla, M., Zhukov, A. N., Berghmans, D., et al. 2022, A&A, 662, L5, doi: 10.1051/0004-6361/202244020

Neergaard-Parker, L., & Zank, G. P. 2012, Astrophys. J., 757, 97, doi: 10.1088/0004-637X/757/1/97

Odstrcil, D. 2003, Advances in Space Research, 32, 497, doi: 10.1016/S0273-1177(03)00332-6

Palmer, I. D. 1982, Rev. Geophys., 20, 335, doi: 10.1029/RG020i002p00335

Parker, E. N. 1965, Plan. Space Sci., 13, 9, doi: 10.1016/0032-0633(65)90131-5

Perri, S., Prete, G., Zimbardo, G., et al. 2023, arXiv e-prints, arXiv:2301.05454, doi: 10.48550/arXiv.2301.05454

Potter, D. 1980, Computational Physics (New York: John Wiley and Sons)

Press, W. H., Flannery, B. P., & Teukolsky, S. A. 1986, Numerical recipes. The art of scientific computing

Prinsloo, P. L., Strauss, R. D., & le Roux, J. A. 2019, ApJ, 878, 144, doi: 10.3847/1538-4357/ab211b

Raouafi, N. E., Matteini, L., Squire, J., et al. 2023, SSRv, 219, 8, doi: 10.1007/s11214-023-00952-4

Reames, D. V. 1999, Space Science Reviews, 90, 413, doi: 10.1023/A:1005105831781

—. 2023, SSRv, 219, 14, doi: 10.1007/s11214-023-00959-x

Reames, D. V., Kahler, S. W., & Ng, C. K. 1997, ApJ, 491, 414, doi: 10.1086/304939

Scholer, M. 1990, Geophys. Res. Lett., 17, 1821, doi: 10.1029/GL017i011p01821

Shu, F. H. 1992, The physics of astrophysics. Volume II: Gas dynamics.

Tan, L. C., Mason, G. M., Gloeckler, G., & Ipavich, F. M. 1989, J. Geophys. Res., 94, 6552, doi: 10.1029/JA094iA06p06552

Wijsen, N., Aran, A., Scolini, C., et al. 2022, A&A, 659, A187, doi: 10.1051/0004-6361/202142698

Winske, D. 1985, AGU Geophys. Monogr. Ser., 35, 225, doi: 10.1029/GM035p0225